




Nitrogen-incorporation activates NiFeO_x catalysts for efficiently boosting oxygen evolution activity and stability of BiVO₄ photoanodes

Beibei Zhang^{1,2}, Shiqiang Yu³, Ying Dai³, Xiaojuan Huang¹, Lingjun Chou¹ [✉], Gongxuan Lu¹ [✉], Guojun Dong¹ & Yingpu Bi^{1,4} [✉]

Developing low-cost and highly efficient catalysts toward the efficient oxygen evolution reaction (OER) is highly desirable for photoelectrochemical (PEC) water splitting. Herein, we demonstrated that N-incorporation could efficiently activate NiFeO_x catalysts for significantly enhancing the oxygen evolution activity and stability of BiVO₄ photoanodes, and the photocurrent density has been achieved up to 6.4 mA cm⁻² at 1.23 V (vs. reversible hydrogen electrode (RHE), AM 1.5 G). Systematic studies indicate that the partial substitution of O sites in NiFeO_x catalysts by low electronegative N atoms enriched the electron densities in both Fe and Ni sites. The electron-enriched Ni sites conversely donated electrons to V sites of BiVO₄ for restraining V⁵⁺ dissolution and improving the PEC stability, while the enhanced hole-attracting ability of Fe sites significantly promotes the oxygen-evolution activity. This work provides a promising strategy for optimizing OER catalysts to construct highly efficient and stable PEC water splitting devices.

¹State Key Laboratory for Oxo Synthesis & Selective Oxidation, National Engineering Research Center for Fine Petrochemical Intermediates, Lanzhou Institute of Chemical Physics, CAS, 730000 Lanzhou, P. R. China. ²University of Chinese Academy of Sciences, 100049 Beijing, P. R. China. ³School of Physics, Shandong University, 250100 Jinan, P. R. China. ⁴Dalian National Laboratory for Clean Energy, CAS, 116023 Dalian, P. R. China. ✉email: ljchou@licp.cas.cn; gxlu@lzb.ac.cn; yingpubi@licp.cas.cn

Photoelectrochemical (PEC) water splitting has been considered as a promising strategy for converting solar light into hydrogen energy^{1–3}. To achieve its practical applications, the design and fabrication of semiconductor photoanodes with sufficient light absorption, effective charge separation, and high surface reactivity are essentially required^{4,5}. Among various candidates, bismuth vanadate (BiVO_4) has been attracted particular attentions owing to its appropriate bandgap (2.4 eV) and suitable band-edge positions^{6–10}. However, suffering from the high charge-recombination and sluggish oxygen evolution reaction (OER) kinetics, most of reported photocurrent densities of BiVO_4 photoanodes are far below the theoretical expectation (7.5 mA cm^{-2} , AM 1.5 G illumination, 100 mW cm^{-2})^{11–13}. During past decades, diverse strategies have been developed to improve the PEC activities of BiVO_4 photoanodes, including elemental doping^{14–16}, facet tailoring^{17–19}, and hetero-junction^{20–24}, etc. Although the PEC performances have been increased to a certain extent owing to the improved carrier mobility as well as electrical conductivity, the intrinsically poor surface reactivity still seriously restricts the PEC conversion efficiency.

Recently, BiVO_4 photoanodes decorated with various transition-metal catalysts have been extensively reported for remarkably promoting the OER activities^{25–29}. Specifically, they could efficiently extract photo-generated holes, minimize over potential, and provide active sites, which are all beneficial to accelerate the PEC water oxidation kinetics. Among various OER catalysts, the VIII metal (Fe, Co, Ni) oxides or (oxy)hydroxides, especially for NiFe-based materials, have attracted particular interests in recent years^{30–34}. For example, Domen et al.³⁵ deposited NiFe bimetallic catalyst on BiVO_4 photoanodes for improving the PEC activities up to 4.2 mA cm^{-2} at $1.23 \text{ V}_{\text{RHE}}$. Zhang and co-workers reported that BiVO_4 photoanodes modified with NiFe complexes exhibited an excellent photocurrent of 5.10 mA cm^{-2} ³¹. Pihosh et al.³⁶ fabricated a $\text{WO}_3/\text{BiVO}_4/\text{CoPi}$ core-shell nanostructured photoanode that achieves near 90% of the theoretical water splitting photocurrent. On this basis, Kosar et al.³⁷ acquired a highly efficient solar-to-hydrogen conversion

efficiency of 7.7% by photovoltaic cell and $\text{WO}_3/\text{BiVO}_4/\text{CoPi}$ core-shell nanorods PEC cell tandem. Despite the crucial roles of OER catalysts for enhancing PEC behaviors have been well established, much less attentions focused on optimizing their electronic structures to further boost the PEC conversion efficiency, especially for bimetallic catalysts.

Herein, we reported the incorporation of non-metallic nitrogen-atom into NiFeO_x catalysts to rationally tailor the electronic structure, which remarkably promoted the photocurrent density of BiVO_4 photoanodes up to 6.4 mA cm^{-2} at $1.23 \text{ V}_{\text{RHE}}$ under AM 1.5 G (100 mW cm^{-2}) with an excellent durability. The outstanding PEC performances should be attributed to the electronic reconstruction in both NiFeO_x and BiVO_4 , resulting from the partial substitution of O sites by low electronegativity N atoms. Specifically, the weak electron-attracting capacity of N atoms led to the electron enrichments on both Fe and Ni sites. Subsequently, the electron injection from Ni atoms to lattice V sites of BiVO_4 was favorable for improving the oxygen-evolution stability, while the Fe sites could effectively attract holes for promoting the PEC activity. This work firstly demonstrates the rational regulation of electronic structures in OER catalysts as well as fundamental understanding of their intrinsic roles in PEC oxygen evolution reaction.

Results

Morphology and structure characterizations. The nanoporous BiVO_4 photoanodes supported on F-doped SnO_2 (FTO) glass substrates were fabricated by an electrochemical deposition associated with calcination treatment¹⁰. Figure 1a shows the scanning electron microscopy (SEM) images of the obtained BiVO_4 photoanodes, clearly revealing their unique worm-like porous structure with an average diameter of 200–300 nm. Additionally, the high-resolution transmission electron microscopy (HR-TEM) image (Supplementary Fig. 1) clearly indicates that these nanocrystals possess a relatively smooth surface and a lattice spacing of 0.311 nm corresponded to (–130) plane of monoclinic BiVO_4 phase. Interestingly, after the decoration of

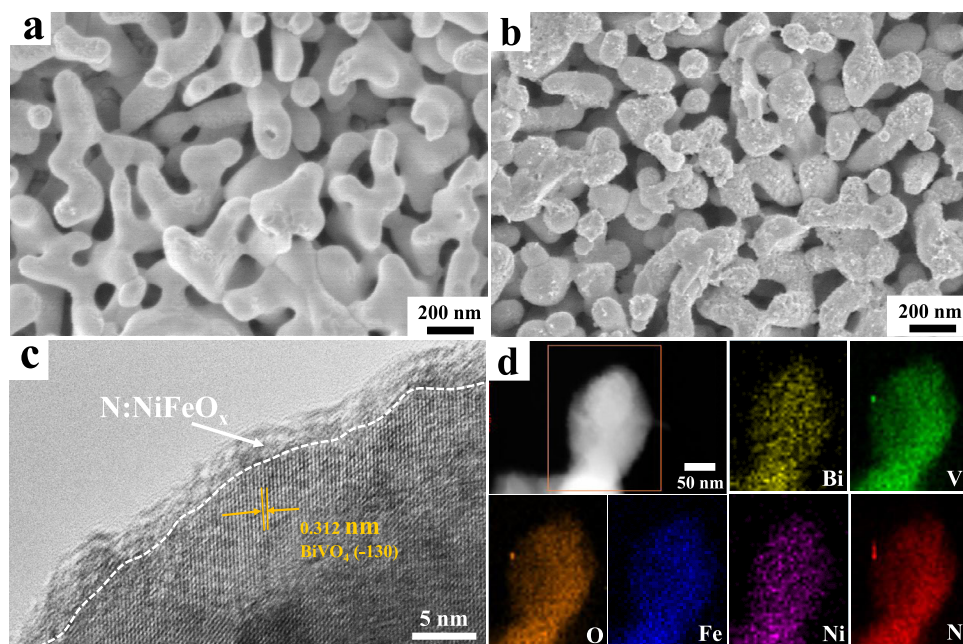


Fig. 1 Morphology and structure characterization of the synthetic photoanodes. SEM images of pristine BiVO_4 (a) and $\text{BiVO}_4/\text{N}:\text{NiFeO}_x$ (b) photoanodes; HR-TEM image (c) and TEM-EDS element mapping analysis (d) of $\text{BiVO}_4/\text{N}:\text{NiFeO}_x$ photoanodes.

N:NiFeO_x catalysts, the smooth surfaces of pristine BiVO₄ photoanodes transformed into a rough flocculent-structure (Fig. 1b). The HR-TEM images (Fig. 1c and Supplementary Fig. 2) clearly indicate that an amorphous layer of N:NiFeO_x catalysts was uniformly covered on BiVO₄ surfaces with a thickness of ~4 nm. Moreover, Fig. 1d and Supplementary Fig. 3 show the energy dispersive spectroscopy (EDS) elemental line and mapping images, revealing the uniform distributions of N, Ni and Fe elements on BiVO₄ crystal surfaces. Besides, the X-ray photoelectron spectroscopy (XPS) result also confirms the successful incorporation of the nitrogen element into the NiFeO_x layer (Supplementary Fig. 4). However, compared with pristine BiVO₄ photoanodes, no evident peak change could be observed in the X-ray diffraction (XRD) patterns after the decoration of N:NiFeO_x catalysts (Supplementary Fig. 5), which should be due to their amorphous structure and ultrathin thickness.

Photoelectrochemical properties. The PEC water splitting performances of N:NiFeO_x catalyst decorated BiVO₄ photoanodes (marked as BiVO₄/N:NiFeO_x) were measured in 0.5 M K₃BO₃ (pH = 9.5) electrolyte under AM 1.5 G illumination (100 mW cm⁻²). For comparison, the PEC activities of pristine BiVO₄ as well as NiFeO_x decorated BiVO₄ photoanodes (marked as BiVO₄/NiFeO_x) have also been studied. As shown in Fig. 2a and Supplementary Fig. 6, the pristine BiVO₄ photoanodes exhibit a relatively low photocurrent density (2.1 mA cm⁻² at 1.23 V_{RHE}), suffering from the sluggish oxygen evolution kinetics at anode/electrolyte interfaces. Obviously, the decoration of NiFeO_x catalysts on BiVO₄ photoanodes could effectively enhance the PEC water oxidation activity, and the photocurrent density has been increased up to 4.4 mA cm⁻² at 1.23 V_{RHE}. Amazingly, an outstanding photocurrent density of 6.4 mA cm⁻² at 1.23 V_{RHE} has been achieved on BiVO₄/N:NiFeO_x photoanodes accompanied by a lower onset potential for OER (Supplementary Fig. 7), clearly indicating that the incorporation of N-atom in NiFeO_x catalysts could significantly promote the oxygen evolution activity (Supplementary Fig. 8 and Figs. 9 and 10).

Furthermore, their maximum half-cell applied bias photon to current efficiencies (HC-ABPE) have been calculated and shown in Fig. 2b. The HC-ABPE value of BiVO₄/N:NiFeO_x photoanode could be achieved up to 1.9% at 0.73 V_{RHE}, which is much higher than that of BiVO₄/NiFeO_x (1.1% at 0.8 V_{RHE}) and pristine BiVO₄ (0.29% at 0.96 V_{RHE}), respectively. Except for the high conversion efficiency, the high stability and durability of photoelectrodes are also required for future practical applications. Figure 2c shows the current-time (*i-t*) curves of these photoanodes operated at 1.23 V_{RHE}. Note that due to the serious photo-corrosion and V⁵⁺ dissolution from crystal lattices, the pristine BiVO₄ exhibited the relatively poor PEC stability and the photocurrent density rapidly decreased^{38–40}. Although the loading of NiFeO_x catalysts on BiVO₄ surfaces could improve the PEC stability to a certain extent, the photocurrent density also decreased down to 2.8 mA cm⁻² after 5 h test. Interestingly, BiVO₄/N:NiFeO_x photoanodes possess the excellent photocurrent stability during the whole test process, indicating the positive effects of N:NiFeO_x on restraining V⁵⁺ dissolution from BiVO₄ lattices and the obtained photoanodes with excellent structural stability (Supplementary Fig. 11, Figs. 12 and 13, and Table 1). The above results clearly reveal that the incorporation of N atoms in NiFeO_x catalysts not only significantly promotes the oxygen evolution activity but also effectively enhances the PEC stability of BiVO₄ photoanodes.

Furthermore, their incident photon to current conversion efficiencies (IPCEs) were conducted and shown in Fig. 2d (Supplementary Fig. 14). At the wavelength of 360 nm, the IPCE values of BiVO₄/N:NiFeO_x photoanodes could be achieved to 93%, which is much higher than BiVO₄ (8%) and BiVO₄/NiFeO_x (54%). Figure 2e shows the electrochemical impedance spectroscopy (EIS) for further elucidating the interfacial charge transfer and oxygen evolution kinetic. According to the Nyquist plots and the fitting results (Supplementary Table 2), the calculated resistance values of BiVO₄/N:NiFeO_x, BiVO₄/NiFeO_x, and BiVO₄ photoanodes were 139.5, 149.8, and 458.9 Ω, respectively, revealing the preferable capability of N:NiFeO_x catalyst for facilitating interface charge transfer. Moreover, the hydrogen and

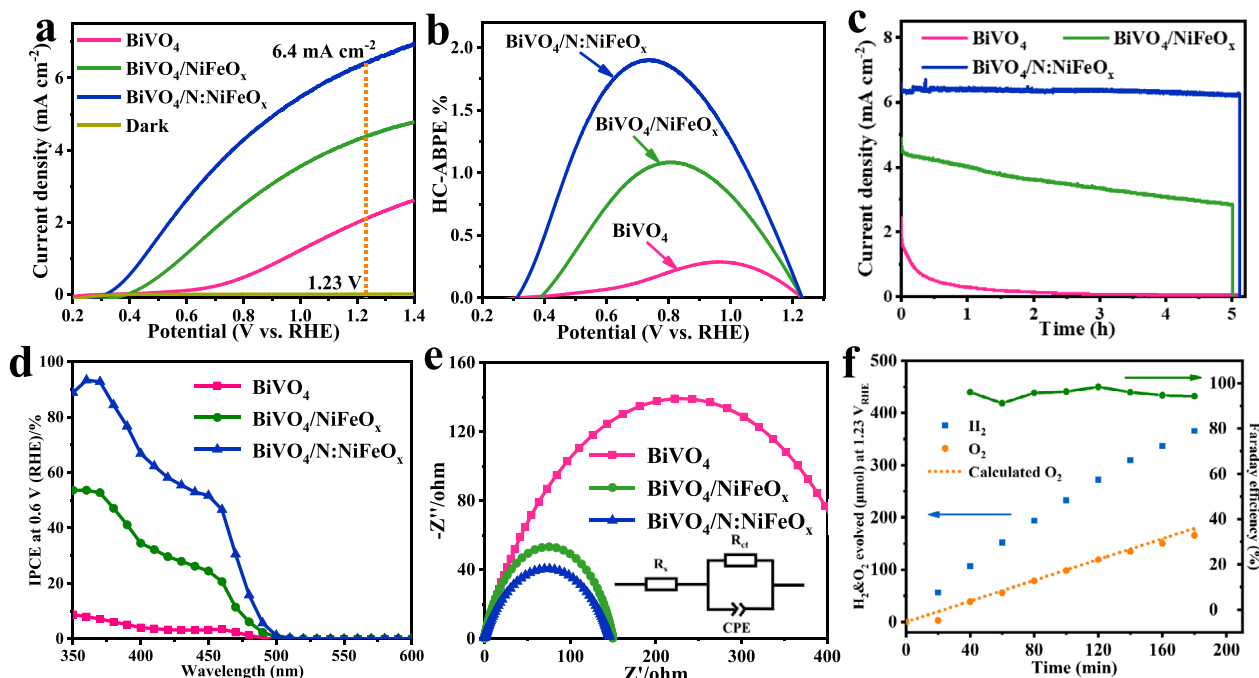


Fig. 2 Photoelectrochemical properties. **a** Linear-sweep voltammograms (LSV, with a scan rate of 10 mV s⁻¹), **b** half-cell ABPE (HC-ABPE) results, **c** *i-t* stability tests measured at 1.23 V vs. RHE, **d** IPCE results at 0.6 V vs. RHE and **e** EIS results at 0.75 V vs. RHE under illumination for BiVO₄, BiVO₄/NiFeO_x, and BiVO₄/N:NiFeO_x photoanodes. **f** H₂ and O₂ evolution of BiVO₄/N:NiFeO_x measured at 1.23 V vs. RHE. All the measurements were carried at 0.5 M K₃BO₃ (pH = 9.5) electrolyte.

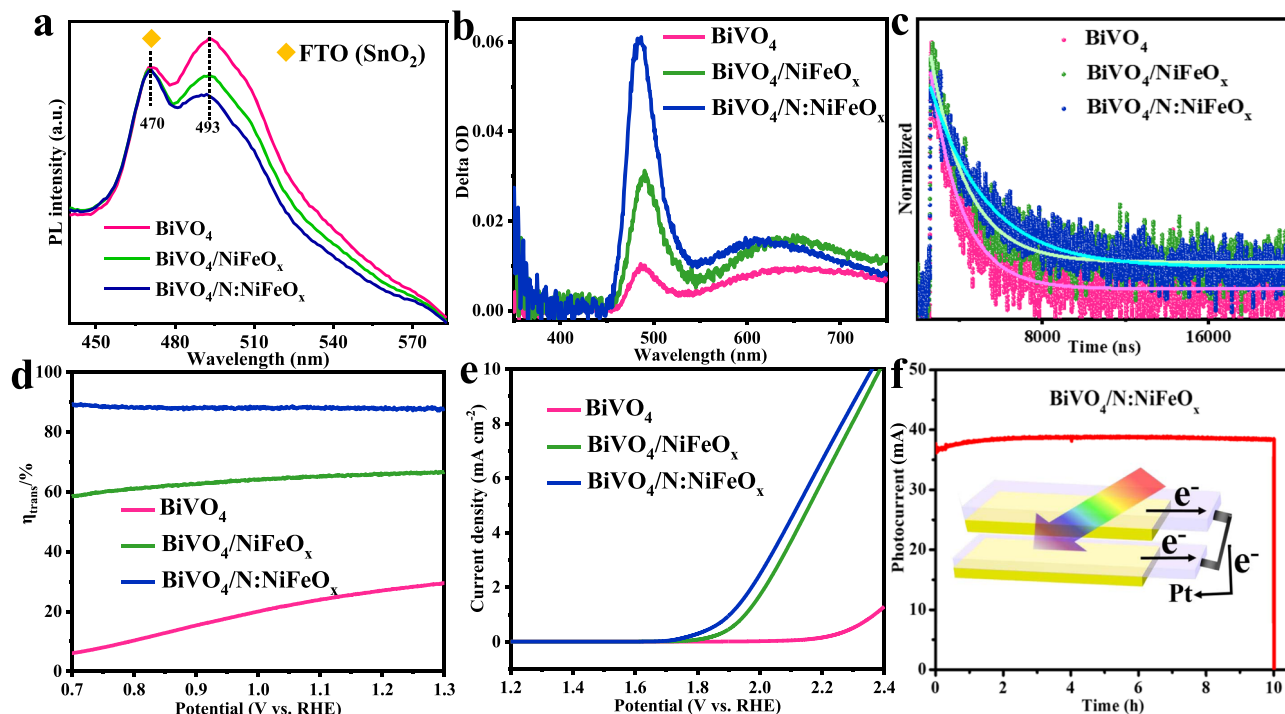


Fig. 3 Spectrum and electrochemical OER properties. **a** PL spectra; **b** transient absorption (TA) spectra; **c** the time-resolved TA curves probed at 490 nm; **d** charge transfer efficiencies (η_{trans}); and **e** LSV curves in the dark of BiVO_4 , $\text{BiVO}_4/\text{NiFeO}_x$, and $\text{BiVO}_4/\text{N}:\text{NiFeO}_x$ photoanodes. **f** I-t curves of the scale-up fabricated $\text{BiVO}_4/\text{N}:\text{NiFeO}_x$ photoanodes ($2 \times 3.5 \text{ cm}^2$) with parallel at $1.23 V_{\text{RHE}}$.

oxygen amounts generated from PEC water splitting over $\text{BiVO}_4/\text{N}:\text{NiFeO}_x$ photoanodes were measured by an online gas chromatography (GC). After 3 h irradiation, the amounts of H_2 and O_2 increased linearly up to 365.3 and 165.8 μmol , respectively (Fig. 2f). Additionally, an average Faradaic efficiency of nearly 95% has been obtained on $\text{BiVO}_4/\text{N}:\text{NiFeO}_x$ photoanodes, further confirming its excellent oxygen evolution capability.

Spectrum and electrochemical analysis. The photoluminescence spectroscopy (PL) has been measured by a fluorescence spectrophotometer under laser excitation of 355 nm. As shown in Fig. 3a, two PL peaks could be clearly identified. More specifically, the peak at 470 nm is associated with FTO (SnO_2) substrate (Supplementary Fig. 15). The peak at 493 nm near the absorption band edge of BiVO_4 (Supplementary Fig. 16) is attributed to radiative recombination of hole in O 2p band and electron in V 3d band, which represents the charge recombination ability^{41,42}. Specifically, the pristine BiVO_4 photoanodes exhibited a very strong PL peak, demonstrating the relatively high electron-hole recombination ratios. However, after the decoration of OER catalysts, the PL peak intensities have been evidently reduced. More specifically, $\text{N}:\text{NiFeO}_x$ catalysts exhibit more efficient capability than NiFeO_x for promoting the charge separation of BiVO_4 photoanodes (Supplementary Fig. 17). Moreover, the time-resolved transient absorption spectra (TR-TAS) have been performed to explore the energy relaxation process and the charge carrier concentrations of the related samples under the excited state^{43–45}. In addition, the decay curves were probed at 490 nm, which was attributed to hole dynamics⁴³. As shown in Fig. 3b, c (Supplementary Table 3), the $\text{BiVO}_4/\text{N}:\text{NiFeO}_x$ photoelectrodes possess higher absorption peak and longer carrier lifetime (2.69 μs) compared with $\text{BiVO}_4/\text{NiFeO}_x$ (1.77 μs) and BiVO_4 (1.51 μs) photoanodes. Based on the above steady/transient spectra analysis, it can be concluded that $\text{N}:\text{NiFeO}_x$ catalysts exhibited the preferable capability for promoting charge

separation and extending the carriers lifetimes. Figure 3d shows their interfacial charge transfer (η_{trans}) efficiencies for water oxidation reaction (Supplementary Fig. 18). The pristine BiVO_4 exhibits a very low efficiency of 28% at $1.23 V_{\text{RHE}}$, while the surface deposition of NiFeO_x and $\text{N}:\text{NiFeO}_x$ catalysts could effectively increase the η_{trans} efficiencies up to 66.3 and 88%, respectively. Furthermore, their electrochemical OER properties under dark conditions have also been studied and shown in Fig. 3e. Obviously, $\text{BiVO}_4/\text{N}:\text{NiFeO}_x$ possesses a lower overpotential and higher water oxidation current compared with BiVO_4 and $\text{BiVO}_4/\text{NiFeO}_x$, further revealing its excellent OER activity. The large-scale fabrication of photoanodes should be necessarily required for future practical applications. Accordingly, the dual $\text{BiVO}_4/\text{N}:\text{NiFeO}_x$ photoanodes with a relatively large area ($2 \times 3.5 \text{ cm}^2$) have been fabricated, and the photocurrent could achieve up to 37 mA at $1.23 V_{\text{RHE}}$ accompanied with an excellent stability of 10 h (Fig. 3f). Thus, the above results clearly demonstrate that the $\text{BiVO}_4/\text{N}:\text{NiFeO}_x$ photoanodes possess the tremendous potential for practical PEC water splitting applications.

Effects of N-incorporation into $\text{BiVO}_4/\text{NiFeO}_x$ films. Furthermore, the effects of the N-incorporation on the surface chemical states and electronic structures of both NiFeO_x and BiVO_4 have been explored by XPS. As shown in Supplementary Figs. 19 and 20, no evident change could be detected in Bi 4f peaks of $\text{BiVO}_4/\text{N}:\text{NiFeO}_x$ compared with $\text{BiVO}_4/\text{NiFeO}_x$ and BiVO_4 , revealing the negligible influence of N-substitution on the Bi sites of BiVO_4 photoanodes. Interestingly, compared with $\text{BiVO}_4/\text{NiFeO}_x$ samples, a shoulder peak at lower binding energy positions could be observed in V 2p spectra of $\text{BiVO}_4/\text{N}:\text{NiFeO}_x$ photoanodes (Fig. 4a), which should be attributed to the formation of $\text{V}^{(5-x)+}$ species. Moreover, the relative ratio of Ni^{3+} species in $\text{BiVO}_4/\text{N}:\text{NiFeO}_x$ has been evidently increased (Fig. 4b)^{46–50}, while the Fe^{3+} ratio has been decreased compared with $\text{BiVO}_4/\text{NiFeO}_x$ samples (Fig. 4c)^{51–53}. On the basis of

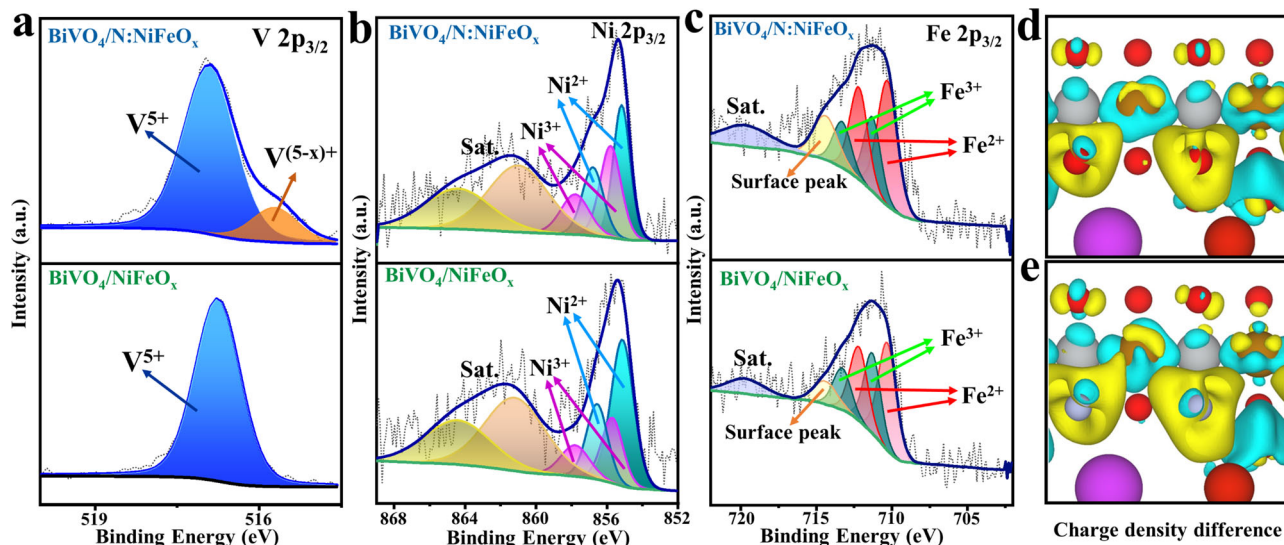


Fig. 4 Effects of N-incorporation on the surface chemical states and electronic structures of $\text{BiVO}_4/\text{NiFeO}_x$. XPS high-resolution **a** V 2p, **b** Ni 2p, and **c** Fe 2p spectra for $\text{BiVO}_4/\text{N:NiFeO}_x$ and $\text{BiVO}_4/\text{NiFeO}_x$ photoanodes, respectively. Schematic of charge density difference (yellow and cyan represent charge accumulation and depletion, respectively; the cut-off of the density-difference isosurface is 0.01 \AA^{-3}) of $\text{BiVO}_4/\text{NiFeO}_x$ (**d**) and $\text{BiVO}_4/\text{N:NiFeO}_x$ (**e**).

above results, it may be proposed that the partial substitution of O sites in NiFeO_x catalysts by N atoms should enrich the electron densities in Fe and Ni sites. Furthermore, the electron-enriched Ni sites conversely donated electrons to V sites of BiVO_4 for restraining V^{5+} dissolution and improving the PEC stability. Additionally, the electron-enriched Fe sites could efficiently attract photo-generated holes from BiVO_4 surfaces, which significantly promoted the oxygen-evolution activity. Thereby, the N-incorporation in NiFeO_x catalysts could effectively promote the oxygen evolution activity and stability of BiVO_4 photoanodes. To further confirm the above speculations, the N atoms in N:NiFeO_x catalysts were replaced by O atoms again via an oxygen plasma treatment. As shown in Supplementary Figs. 20 and 21, all the XPS peaks of Fe, Ni, Bi, and V elements were nearly consistent with $\text{BiVO}_4/\text{NiFeO}_x$ photoanodes. Additionally, after the replacement of N with O atoms, the photocurrent density has been obviously reduced from 6.4 to 5 mA cm^{-2} at $1.23V_{\text{RHE}}$ accompanied by the poor PEC water oxidation stability (Supplementary Fig. 22), confirming the crucial roles of N-incorporation in promoting the OER activity and PEC stability of BiVO_4 photoanodes.

DFT calculation and analysis. Furthermore, the density functional theory (DFT) calculation has been performed to reveal the change of electron densities in Fe and Ni sites after incorporation of N atoms. As shown in Fig. 4d, e, the charge density difference results clearly reveal that the electron densities at Fe and Ni sites increased significantly (yellow regions) after partial substitution of O sites with N atoms in NiFeO_x catalysts. Additionally, the Bader charge analysis (Supplementary Table 4) also verified the enriched electron densities with the N-incorporation, which is highly consistent with the XPS results. Thereby, these calculation results could further provide supports on the crucial roles of N-incorporation in regulating the electronic structures of NiFeO_x .

Discussion

In summary, we reported a facile N-incorporation method to rationally regulate the electronic structures of NiFeO_x catalyst decorated on BiVO_4 photoanodes. More detailed experiments and XPS analysis reveal that owing to the relatively low electronegativity of N atoms, their incorporation in NiFeO_x catalysts facilitates the electron enrichments in Fe and Ni sites.

Furthermore, the Ni sites would donate electrons to V sites on BiVO_4 surface, which could efficiently restrain V^{5+} dissolution and improve the PEC water oxidation stability. Moreover, the enhanced hole-attracting ability of Fe sites significantly promotes the oxygen-evolution activity. As expected, the $\text{BiVO}_4/\text{N:NiFeO}_x$ photoanodes exhibited an outstanding photocurrent density of 6.4 mA cm^{-2} at $1.23 V_{\text{RHE}}$ (AM 1.5 G, 100 mW cm^{-2}) accompanying with the enhanced PEC stability. This work provides a new insight to construct highly efficient and stable OER catalysts for fabricating high-efficiency PEC devices.

Methods

Materials. All chemicals were of analytical grade purity, obtained from Sinopharm Chemical Reagent Co., Ltd., and used as received without further purification. Deionized water (Molecular Corp., $18.25 \text{ M}\Omega \text{ cm}$) used in the synthesis was from local sources.

Synthesis of nanoporous BiVO_4 photoanodes. The nanoporous BiVO_4 photoanode was obtained based on the previous report¹⁰. $2 \text{ mM Bi(NO}_3)_3 \cdot 5\text{H}_2\text{O}$ was dissolved in 0.4 M KI solution (50 mL). Then, the pH value of this solution was adjusted to 1.7 by HNO_3 . Subsequently, 0.23 M quinhydrone was dispersed into ethanol solution (20 mL). Finally, mixing the two solution and stirring vigorously for a few minutes to acquire the electrodeposited solution. The cathodic deposition was performed at a constant potential of -0.1 V vs. Ag/AgCl for 3 min at room temperature to obtain the BiOI electrodes, among which FTO, Ag/AgCl (4 M KCl), and platinum pair were used as working electrode (WE), reference electrode (RE) and counter electrode (CE), respectively. Then, $\text{VO}(\text{acac})_2$ (0.2 M , 0.2 mL) dissolved in DMSO (10 mL) solution was coated on the BiOI electrodes and heated in the air in a muffle furnace at $450 \text{ }^\circ\text{C}$ for 2 h (ramping rate = $2 \text{ }^\circ\text{C/min}$) to convert to BiVO_4 . After calcination, the excess V_2O_5 on the electrode surface was soaked into NaOH (1 M) solution for 15 min to remove. Finally, the electrodes were rinsed with deionized water and dried in air to obtain pure BiVO_4 photoanodes.

Synthesis of $\text{BiVO}_4/\text{NiFeO}_x$ and $\text{BiVO}_4/\text{N:NiFeO}_x$ photoanodes. The as-prepared BiVO_4 electrodes were immersed into the freshly mixed metal salt solution (pH ~ 2.8) for 15 min (2.5 mL of $10 \text{ mM FeCl}_3 \cdot 6\text{H}_2\text{O}$ and 7.5 mL of $10 \text{ mM NiCl}_2 \cdot 6\text{H}_2\text{O}$). Then, 2 M NaOH solution was added to adjust its pH to ~ 8 (The electrodes were still kept in this mixed solution during pH adjustment process). Subsequently, the solution was stood for 50 min and maintained at $25 \text{ }^\circ\text{C}$ throughout the co-catalyst loading process. Finally, the electrodes were washed by deionized water and calcined at $300 \text{ }^\circ\text{C}$ for 1 h in a muffle furnace in air atmosphere to obtain the $\text{BiVO}_4/\text{NiFeO}_x$ samples. The synthesis of $\text{BiVO}_4/\text{N:NiFeO}_x$ and $\text{BiVO}_4/\text{O}_2\text{-NiFeO}_x$ photoanodes was the same as the above steps for the preparation of $\text{BiVO}_4/\text{NiFeO}_x$, except that the final calcination process is changed to a N_2 or O_2 plasma treatment for 5 min (a medium power of 10.5 W and a pressure of

300 Pa, Supplementary Fig. 23). The BiVO₄/N:BiFeO_x-O₂ photoanodes were prepared via an oxygen plasma treatment BiVO₄/N:BiFeO_x for 5 min.

Synthesis of BiVO₄/NiFeP and BiVO₄/NiFeB photoanodes. The BiVO₄ photoanodes were immersed into the fresh metal salt solution (2.5 mL of 10 mM FeCl₃·6H₂O and 7.5 mL of 10 mM NiCl₂·6H₂O), and then a NaBH₄ aqueous solution was added dropwise. The solution was stood for 50 min. Finally, the electrodes were washed by deionized water to obtain the BiVO₄/NiFeB photoanodes. Firstly, the BiVO₄ films were dipped into a water solution (20 mL) A containing SnCl₂ (0.8 g) and HCl (40 wt%, 0.8 mL) for 2 min. Secondly, the films were further immersed into a water solution (20 mL) B of PdCl₂ (10 mM, 3.4 mL), HF (40–50 wt%, 0.16 mL) and HCl (40 wt%, 0.2 mL) for 2 min. Finally, the films were immersed into the solution C at 60 °C for 40 s and then rinsed with deionized water to obtain the BiVO₄/NiFeP photoanodes. The water solution (20 mL) C contains NiSO₄·6H₂O (0.15 g), FeSO₄·4H₂O (0.15 g), NH₄F (0.2 g), NaH₂-PO₂·H₂O (0.8 g), and Na₃C₆H₅O₇·2H₂O (0.4 g), and the value of pH was further adjusted to 9.0 by adding ammonia⁵⁴.

Measurement and characterization. Scanning electron microscopy measurements were carried out on a field-emission scanning electron microscope (SEM, SU8020). Transmission electron microscopy (TEM) measurements were performed by using a FEI Tecnai TF20 microscope operated at 200 kV. The elemental composition and chemical valence states were explored by X-ray photoelectron spectroscopy (XPS, Al-Kα, 1486.6 eV, ESCALAB 250Xi). The crystalline structures were identified by X-ray diffraction analysis (XRD, Smartlab-SE). UV-visible diffuse reflectance spectra were performed on a UV-2550 (Shimadzu) spectrometer by using BaSO₄ as the reference.

Spectrum measurements. The photoluminescence (PL) spectra were tested on F-7000 fluorescence spectrophotometer (Hitachi, Tokyo Japan) under laser excitation of 355 nm. The time-resolved transient absorption (TA) spectra were performed on LP980 spectrometer (Edinburgh Instruments Ltd., model LP980), combined with a compact Q-switched Nd:YAG laser (Continuum, the USA). The probe source was a 150 W pulsed Xenon lamp for kinetic and spectral studies. The measurements were achieved with single-flash laser excitation at 355 nm (10 Hz, FWHM~7 ns) as the pump source. The kinetic traces and transient absorption spectra were collected with a Hamamatsu R928 photomultiplier tube detector (PMT) and an iStar ICCD camera (Andor Technology), respectively. The samples were placed in a film holder, which is suitable for semi-transparent materials. The obtained data were analyzed with the Edinburgh software (LP900). In addition, the decay curves were probed at 490 nm (Fig. 3c), and their fitting was based on a biexponential decay model according to the following equation and the fitting parameters have been listed in Supplementary Table 3.

$$R(t) = B_1 e^{-\frac{t}{\tau_1}} + B_2 e^{-\frac{t}{\tau_2}} \quad (1)$$

Photoelectrochemical measurements. The photoelectrochemical measurement was carried out on an electrochemical workstation (CHI760E) in a standard three-electrode system and a 0.5 M K₃BO₃ electrolyte (pH = 9.5) under AM 1.5 G simulated sunlight (100 mW cm⁻²). A dual-channel power and energy meters (PM320E, THORLABS) equipped with high-sensitivity S310C probe (THORLABS) was used to calibrate the AM 1.5 light intensity to 100 mW/cm². Moreover, the solar simulator used in our experiments has been equipped with a total-reflection mirror and AM 1.5 G filter for PEC measurements and the corresponding spectrum has been measured by a spectrometer (BLUE-Wave, StellarNet) and shown in Supplementary Fig. 24. The photocurrent vs. voltage (*J*-*V*) characteristics were determined by scanning potential from -0.6 to 1.0 V (vs. Ag/AgCl) with a scan rate of 10 mV s⁻¹ and the applied potentials could be converted into reversible hydrogen electrode (RHE) using the Nernst equation:

$$E_{\text{RHE}} = E_{\text{Ag/AgCl}} + 0.059\text{pH} + 0.197(25^\circ\text{C}) \quad (2)$$

The incident photon to current efficiency (IPCE) was determined using a full solar simulator (Newport, Model 9600, 300 W Xe arc lamp) and a motorized monochromator (Oriol Cornerstone 130 1/8 m) at 0.6 V_{RHE} in a 0.5 M K₃BO₃ electrolyte. The IPCE result was calculated using the equation⁵⁵:

$$\text{IPCE}(\%) = \frac{1240 \times I(\text{mA}/\text{cm}^2)}{P_{\text{light}}(\text{mW}/\text{cm}^2) \times \lambda(\text{nm})} \times 100 \quad (3)$$

where *I* is the measured photocurrent density at specific wavelength, *λ* is the wavelength of incident light, and *P*_{light} is the measured light power density at that wavelength.

Supposing 100% Faradaic efficiency, the half-cell applied bias photon-to-current efficiency (HC-ABPE) was calculated by following equation⁵⁵:

$$(\text{HC} - \text{ABPE})(\%) = \frac{I(\text{mA}/\text{cm}^2) \times (1.23 - V_{\text{bias}})(\text{V})}{P_{\text{light}}(\text{mW}/\text{cm}^2)} \times 100 \quad (4)$$

where *I* is the photocurrent density, *V*_{bias} is the applied potential, and *P*_{light} is the incident illumination power density (100 mW cm⁻²).

The electrochemical impedance spectroscopy (EIS) Nyquist plots were obtained at 0.75 V (vs. RHE) with a small AC amplitude of 10 mV in the frequency range of 10⁻² to 10⁵ Hz and the measured spectra were fitted with Zview software.

Surface charge transfer efficiencies (*η*_{trans}) of BiVO₄, BiVO₄/NiFeO_x, and BiVO₄/N:BiFeO_x photoanodes can be calculated using the following equation⁵⁶:

$$\eta_{\text{trans}} = \frac{J^{\text{H}_2\text{O}}}{J^{\text{H}_2\text{O}_2}} \quad (5)$$

J^{H₂O} and *J*^{H₂O₂} are the photocurrent densities obtained in 0.5 M potassium borate electrolytes (pH 9.5) without and with H₂O₂, respectively. Additionally, a summary of recent significant progress of BiVO₄-based photoanodes has been reviewed (Supplementary Table 5).

The evolution of H₂ and O₂ was performed in a 0.5 M K₃BO₃ electrolyte at 1.23 V_{RHE} under AM 1.5 G illumination (100 mW cm⁻²) by an online gas analysis system (Labsolar 6 A, Beijing Perfect light Technology Co. Ltd.) and a gas chromatograph (GC 7890 A, Agilent Technologies).

The PEC performances of two parallel BiVO₄/N:BiFeO_x photoanodes (single area: 2 × 3.5 cm², distance: ~1 cm) were performed at 1.23 V_{RHE} in 0.5 M K₃BO₃. Specifically, the simulated solar light illuminates vertically these two photoanodes, which were connected with copper wires.

Computational method. The Vienna Ab Initio Simulation Package (VASP) code described by the projector augmented wave (PAW) method for ion-electron interaction was applied to the simulation calculations^{57,58}. The generalized gradient approximation (GGA) expressed in the form of the Perdew-Burke-Ernzerhof (PBE) function was used to deal with exchange-correlation interactions⁵⁹. The cutoff energy of 500 eV was taken into account by all calculations, and the Monkhorst-Pack *k*-point grid was set to 3 × 3 × 3 for bulk structure optimization, 5 × 5 × 1 for BiVO₄(001)/NiFeO_x and BiVO₄(001)/N:BiFeO_x heterostructures. The empirical correction scheme of Grimme (DFT+D2) was adopted for considering van der Waals (vdW) interaction⁶⁰. The convergence criterion for Hellmann-Feynman forces and total energy were set to 0.01 eV/Å and 10⁻⁵ eV, and the vacuum space in the *z*-direction was greater than 20 Å to avoid the interaction between adjacent units during structural relaxation. A twelve atomic layers BiVO₄ (001) slab model was used, and the bottom six atomic layers were fixed to simulate the bulk structure.

Data availability

Data reported in the main article are provided in the Source Data file. The remaining data that support the findings of this study are available from the corresponding author upon request. Source data are provided with this paper.

Received: 8 February 2021; Accepted: 11 November 2021;

Published online: 29 November 2021

References

- Bard, A. J. Photoelectrochemistry. *Science* **207**, 139–144 (1980).
- Tryk, D. A., Fujishima, A. & Honda, K. Recent topics in photoelectrochemistry: achievements and future prospects. *Electrochim. Acta* **45**, 2363–2376 (2000).
- Pinaud, B. A. et al. Technical and economic feasibility of centralized facilities for solar hydrogen production via photocatalysis and photoelectrochemistry. *Energy Environ. Sci.* **6**, 1983–2002 (2013).
- Döscher, H., Geisz, J. F., Deutsch, T. G. & Turner, J. A. Sunlight absorption in water - efficiency and design implications for photoelectrochemical devices. *Energy Environ. Sci.* **7**, 2951–2956 (2014).
- Li, J. & Wu, N. Semiconductor-based photocatalysts and photoelectrochemical cells for solar fuel generation: a review. *Catal. Sci. Technol.* **5**, 1360–1384 (2015).
- Wolcott, A., Smith, W. A., Kuykendall, T. R., Zhao, Y. & Zhang, J. Z. Photoelectrochemical study of nanostructured ZnO thin films for hydrogen generation from water splitting. *Adv. Funct. Mater.* **19**, 1849–1856 (2009).
- Zhang, P., Yu, L. & Lou, X. W. Construction of heterostructured Fe₂O₃-TiO₂ microdumbbells for photoelectrochemical water oxidation. *Angew. Chem. Int. Ed.* **57**, 15076–15080 (2018).
- Zhong, D. K. & Gamelin, D. R. Photoelectrochemical water oxidation by cobalt catalyst (“Co–Pi”)/α-Fe₂O₃ composite photoanodes: oxygen evolution and resolution of a kinetic bottleneck. *J. Am. Chem. Soc.* **132**, 4202–4207 (2010).
- Wang, G. et al. Hydrogen-treated TiO₂ nanowire arrays for photoelectrochemical water splitting. *Nano Lett.* **11**, 3026–3033 (2011).
- Kim, T. W. & Choi, K.-S. Nanoporous BiVO₄ photoanodes with dual-layer oxygen evolution catalysts for solar water splitting. *Science* **343**, 990–994 (2014).

11. Prasad, U. et al. Role of alkali metal in BiVO₄ crystal structure for enhancing charge separation and diffusion length for photoelectrochemical water splitting. *ACS Appl. Mater. Interfaces* **12**, 52808–52818 (2020).
12. Wang, S., Chen, P., Yun, J. H., Hu, Y. & Wang, L. An electrochemically treated BiVO₄ photoanode for efficient photoelectrochemical water splitting. *Angew. Chem. Int. Ed.* **56**, 8500–8504 (2017).
13. Gan, J. et al. Efficient photoelectrochemical water oxidation over hydrogen-reduced nanoporous BiVO₄ with Ni-Bi electrocatalyst. *ChemElectroChem* **2**, 1385–1395 (2015).
14. Jo, W. J. et al. Phosphate doping into monoclinic BiVO₄ for enhanced photoelectrochemical water oxidation activity. *Angew. Chem. Int. Ed.* **51**, 3147–3151 (2012).
15. Tayebi, M. & Lee, B.-K. The effects of W/Mo-co-doped BiVO₄ photoanodes for improving photoelectrochemical water splitting performance. *Catal. Today* **361**, 183–190 (2021).
16. Luo, W. et al. Formation energy and photoelectrochemical properties of BiVO₄ after doping at Bi³⁺ or V⁵⁺ sites with higher valence metal ions. *Phys. Chem. Chem. Phys.* **15**, 1006–1013 (2013).
17. Wang, S., Liu, G. & Wang, L. Crystal facet engineering of photoelectrodes for photoelectrochemical water splitting. *Chem. Rev.* **119**, 5192–5247 (2019).
18. Zhou, C. et al. A facet-dependent schottky-junction electron shuttle in a BiVO₄{010}-Au-Cu₂O Z-scheme photocatalyst for efficient charge separation. *Adv. Funct. Mater.* **28**, 1801214 (2018).
19. Han, H. S. et al. Boosting the solar water oxidation performance of a BiVO₄ photoanode by crystallographic orientation control. *Energy Environ. Sci.* **11**, 1299–1306 (2018).
20. Rao, P. M. et al. Simultaneously efficient light absorption and charge separation in WO₃/BiVO₄ core/shell nanowire photoanode for photoelectrochemical water oxidation. *Nano Lett.* **14**, 1099–1105 (2014).
21. Chang, X. et al. Enhanced surface reaction kinetics and charge separation of p-n heterojunction Co₃O₄/BiVO₄ photoanodes. *J. Am. Chem. Soc.* **137**, 8356–8359 (2015).
22. Ye, K.-H. et al. Enhancing photoelectrochemical water splitting by combining work function tuning and heterojunction engineering. *Nat. Commun.* **10**, 3687 (2019).
23. Liu, Y. et al. Facet effect on the photoelectrochemical performance of a WO₃/BiVO₄ heterojunction photoanode. *Appl. Catal. B Environ.* **245**, 227–239 (2019).
24. Phiankoh, S., Prajongtat, P., Chareonpanich, M. & Munprom, R. The improved photoelectrochemical performance of WO₃/BiVO₄ heterojunction thin-film photoanodes via thermal treatment. *Energy Technol.* **8**, 2000147 (2020).
25. Wang, S. et al. New iron-cobalt oxide catalysts promoting BiVO₄ films for photoelectrochemical water splitting. *Adv. Funct. Mater.* **28**, 1802685 (2018).
26. Saada, H. et al. Boosting the performance of BiVO₄ prepared through alkaline electrodeposition with an amorphous Fe Co-catalyst. *ChemElectroChem* **6**, 613–617 (2019).
27. She, H. et al. Fabrication of BiVO₄ photoanode cocatalyzed with NiCo-layered double hydroxide for enhanced photoactivity of water oxidation. *Appl. Catal. B Environ.* **263**, 118280 (2020).
28. Zhong, D. K., Choi, S. & Gamelin, D. R. Near-complete suppression of surface recombination in solar photoelectrolysis by “Co-Pi” catalyst-modified W:BiVO₄. *J. Am. Chem. Soc.* **133**, 18370–18377 (2011).
29. He, W. et al. Enhanced photoelectrochemical water oxidation on a BiVO₄ photoanode modified with multi-functional layered double hydroxide nanowalls. *J. Mater. Chem. A* **3**, 17977–17982 (2015).
30. Zhang, B. et al. Unveiling the activity and stability origin of BiVO₄ photoanodes with FeNi oxyhydroxides for oxygen evolution. *Angew. Chem. Int. Ed.* **59**, 18990–18995 (2020).
31. Shi, Y. et al. Boosting photoelectrochemical water oxidation activity and stability of Mo-doped BiVO₄ through the uniform assembly coating of NiFe-phenolic networks. *ACS Energy Lett.* **3**, 1648–1654 (2018).
32. Wang, S. et al. In situ formation of oxygen vacancies achieving near-complete charge separation in planar BiVO₄ photoanodes. *Adv. Mater.* **32**, 2001385 (2020).
33. Cai, L. et al. One-step hydrothermal deposition of Ni:FeOOH onto photoanodes for enhanced water oxidation. *ACS Energy Lett.* **1**, 624–632 (2016).
34. Li, L. et al. Serial hole transfer layers for a BiVO₄ photoanode with enhanced photoelectrochemical water splitting. *Nanoscale* **10**, 18378–18386 (2018).
35. Kuang, Y. et al. A front-illuminated nanostructured transparent BiVO₄ photoanode for >2% efficient water splitting. *Adv. Energy Mater.* **6**, 1501645 (2016).
36. Pihosh, Y. et al. Photocatalytic generation of hydrogen by core-shell WO₃/BiVO₄ nanorods with ultimate water splitting efficiency. *Sci. Rep.* **5**, 11141 (2015).
37. Kosar, S. et al. Highly efficient photocatalytic conversion of solar energy to hydrogen by WO₃/BiVO₄ core-shell heterojunction nanorods. *Appl. Nanosci.* **9**, 1017–1024 (2019).
38. Lee, D. K. & Choi, K. S. Enhancing long-term photostability of BiVO₄ photoanodes for solar water splitting by tuning electrolyte composition. *Nat. Energy* **3**, 53–60 (2018).
39. Kuang, Y. et al. Ultraportable low-bias water splitting photoanodes via photocorrosion inhibition and in situ catalyst regeneration. *Nat. Energy* **2**, 16191 (2017).
40. Berglund, S. P., Flaherty, D. W., Hahn, N. T., Bard, A. J. & Mullins, C. B. Photoelectrochemical oxidation of water using nanostructured BiVO₄ films. *J. Phys. Chem. C* **115**, 3794–3802 (2011).
41. Kudo, A., Omori, K. & Kato, H. A novel aqueous process for preparation of crystal form-controlled and highly crystalline BiVO₄ powder from layered vanadates at room temperature and its photocatalytic and photophysical properties. *J. Am. Chem. Soc.* **121**, 11459–11467 (1999).
42. Gu, S. et al. Synthesis of buckhorn-like BiVO₄ with a shell of CeO_x nanodots: Effect of heterojunction structure on the enhancement of photocatalytic activity. *Appl. Catal. B Environ.* **170**, 186–194 (2015).
43. Ma, Y., Pendlebury, S. R., Reynal, A., Formal, F. L. & Durrant, J. R. Dynamics of photogenerated holes in undoped BiVO₄ photoanodes for solar water oxidation. *Chem. Sci.* **5**, 2964–2973 (2014).
44. Grigioni, I., Stamplescokie, K. G., Selli, E. & Kamat, P. V. Dynamics of photogenerated charge carriers in WO₃/BiVO₄ heterojunction photoanodes. *J. Phys. Chem. C* **119**, 20792–20800 (2015).
45. Cooper, J. K. et al. Physical origins of the transient absorption spectra and dynamics in thin-film semiconductors: the case of BiVO₄. *J. Phys. Chem. C* **122**, 20642–20652 (2018).
46. Biesinger, M. C. et al. Resolving surface chemical states in XPS analysis of first row transition metals, oxides and hydroxides: Cr, Mn, Fe, Co and Ni. *Appl. Surf. Sci.* **257**, 2717–2730 (2011).
47. Biesinger, M. C., Payne, B. P., Lau, L. W. M., Gerson, A. & Smart, R. S. C. X-ray photoelectron spectroscopic chemical state quantification of mixed nickel metal, oxide and hydroxide systems. *Surf. Interf. Anal.* **41**, 324–332 (2009).
48. Grosvenor, A. P., Biesinger, M. C., Smart, R. S. C. & McIntyre, N. S. New interpretations of XPS spectra of nickel metal and oxides. *Surf. Sci.* **600**, 1771–1779 (2006).
49. Salunkhe, P., Ali, A., V., M. & Kekuda, D. Investigation on tailoring physical properties of Nickel Oxide thin films grown by dc magnetron sputtering. *Mater. Res. Express* **7**, 016427 (2020).
50. Zhu, L. et al. Synthesis of novel platinum-on-flower-like nickel catalysts and their applications in hydrogenation reaction. *Appl. Surf. Sci.* **423**, 836–844 (2017).
51. Elmi, C., Guggenheim, S. & Giere, R. Surface crystal chemistry of phyllosilicates using X-ray photoelectron spectroscopy: a review. *Clays Clay Miner.* **64**, 537–551 (2016).
52. Claros, M., Setka, M., Jimenez, Y. P. & Vallejos, S. AACVD synthesis and characterization of iron and copper oxides modified ZnO structured films. *Nanomaterials* **10**, 471 (2020).
53. Grosvenor, A. P., Kobe, B. A., Biesinger, M. C. & McIntyre, N. S. Investigation of multiplet splitting of Fe 2p XPS spectra and bonding in iron compounds. *Surf. Interface Anal.* **36**, 1564–1574 (2004).
54. Li, F. et al. Electroless plating of NiFeP alloy on the surface of silicon photoanode for efficient photoelectrochemical water oxidation. *ACS Appl. Mater. Interfaces* **12**, 11479–11488 (2020).
55. Chen, Z. et al. Accelerating materials development for photoelectrochemical hydrogen production: Standards for methods, definitions, and reporting protocols. *J. Mater. Res.* **25**, 3–16 (2010).
56. Dotan, H., Sivula, K., Grätzel, M., Rothschild, A. & Warren, S. C. Probing the photoelectrochemical properties of hematite (α-Fe₂O₃) electrodes using hydrogen peroxide as a hole scavenger. *Energy Environ. Sci.* **4**, 958–964 (2011).
57. Kresse, G. & Furthmüller, J. Efficient iterative schemes for ab initio total-energy calculations using a plane-wave basis set. *Phys. Rev. B Condens. Matter Mater. Phys.* **54**, 11169 (1996).
58. Kresse, G. & Joubert, D. From ultrasoft pseudopotentials to the projector augmented-wave method. *Phys. Rev. B Condens. Matter Mater. Phys.* **59**, 1758–1775 (1999).
59. Perdew, J. P., Burke, K. & Ernzerhof, M. Generalized Gradient Approximation Made Simple. *Phys. Rev. Lett.* **77**, 3865 (1996).
60. Grimme, S. Semiempirical GGA-type density functional constructed with a long-range dispersion correction. *J. Comput. Chem.* **27**, 1787–1799 (2006).

Acknowledgements

The work was supported by the National Natural Science Foundation of China (21832005), the China National Key Research and Development Plan Project (No. 2018YFB1502000), and the DNL Cooperation Fund CAS (DNL201922).

Author contributions

B.Z. and Y.B. conceived and designed experiments. L.C. and G.L. directed the experiments and revised the paper. B.Z. performed the measurements. S.Y. and Y.D. carried out the theoretical simulation. X.H. performed the XPS measurement and G.D. performed the SEM measurements. B.Z. and Y.B. wrote the paper. All authors reviewed the paper.

Competing interests

The authors declare no competing interests.

Additional information

Supplementary information The online version contains supplementary material available at <https://doi.org/10.1038/s41467-021-27299-0>.

Correspondence and requests for materials should be addressed to Lingjun Chou, Gongxuan Lu or Yingpu Bi.

Peer review information *Nature Communications* thanks Štěpán Kment, Yuriy Pihosh and the other, anonymous, reviewer(s) for their contribution to the peer review of this work.

Reprints and permission information is available at <http://www.nature.com/reprints>

Publisher's note Springer Nature remains neutral with regard to jurisdictional claims in published maps and institutional affiliations.



Open Access This article is licensed under a Creative Commons Attribution 4.0 International License, which permits use, sharing, adaptation, distribution and reproduction in any medium or format, as long as you give appropriate credit to the original author(s) and the source, provide a link to the Creative Commons license, and indicate if changes were made. The images or other third party material in this article are included in the article's Creative Commons license, unless indicated otherwise in a credit line to the material. If material is not included in the article's Creative Commons license and your intended use is not permitted by statutory regulation or exceeds the permitted use, you will need to obtain permission directly from the copyright holder. To view a copy of this license, visit <http://creativecommons.org/licenses/by/4.0/>.

© The Author(s) 2021